RSC Advances

ROYAL SOCIETY OF CHEMISTRY

REVIEW

View Article Online
View Journal | View Issue

Check for updates

Cite this: *RSC Adv.*, 2025, **15**, 13812

Colloidal quantum dots: surface and interface engineering for light-driven hydrogen production

Mengke Cai, †*[ab] Shuai Huang,†[a] Yimin You,[a] Haotian Jiang,[a] Jing Qiu,[a] Wei Zhang,[a] Qiang Xu,[a] Si Shen,[a] Weiying Hu,[a] Shijie Deng,[a] Zhuojian Li,[b] Xin Tong*[bc] and Hai-Zhi Song*[abcd]

Received 8th January 2025
Accepted 14th April 2025

DOI: 10.1039/d5ra00179j

rsc.li/rsc-advances

Solar energy is the most abundant and clean energy resource for the production of hydrogen, which is inexpensive but requires robust semiconductors. Colloidal quantum dots (CQDs) are considered an ideal semiconductor for hydrogen production. Although light-driven hydrogen production systems have been explored for multifarious CQD-based materials and devices, a comprehensive summary on surface and interface engineering has been rarely reported. In this review, we discuss the surface and interface modification strategies for CQD-based light-driven hydrogen production and emphasize on direct light-driven hydrogen generation systems categorized into photoelectrochemical cells and photocatalysis systems. Furthermore, we describe the recent research advances in this growing field by highlighting various strategies developed for the optimization of surface and interface characteristics, such as core–shell structural design, passivation layer modification, surface ligand optimization, heterostructure construction, co-catalyst loading, and defect engineering. Finally, a future outlook on and the challenges in surface and interface regulation of CQD-based light-driven hydrogen production systems are highlighted. It is expected that this review will stimulate continued interest in harnessing the significant potential of CQDs for solar-to-hydrogen conversion.

1. Introduction

In order to meet the increasing demand for sustainable and clean energy in human society, light-driven hydrogen production technology provides a promising approach, which can directly convert solar energy into hydrogen with the highest energy density per unit mass and clean characteristics.[1,2] Light-driven hydrogen production technology mainly includes photoelectrochemical and photocatalytic systems, both of which rely on semiconductor materials for driving solar-to-hydrogen conversion.[3,4] Colloidal quantum dots (CQDs) have unique optical and electronic properties owing to their quantum effects.[5] In addition, because of their high surface atomic proportion and specific surface area, their surface effects are more pronounced. Hence, CQDs are regarded as potential semiconductor materials for the development of light-driven hydrogen production technology.[6]

Although CQDs exhibit more pronounced quantum and surface properties than macroscopic semiconductor materials,[7] CQDs have relatively poor photostability and chemical stability owing to their colloidal properties.[8] Moreover, the most commonly used CQDs are binary II–VI and IV–VI CQDs containing toxic heavy metals such as Cd and Pb. Considering the future industrial scale and environmental pollution issues in the field of light-driven hydrogen production, enhancing photostability and chemical stability have become a key focus.[9] In addition, there are a large number of defects formed on the surface of CQDs during the colloidal synthesis process, which lead to the recombination of photo-generated carriers on their surface.[10]

All of the above problems limit the further development of CQDs for light-driven hydrogen production.[11] Fortunately, the understanding of the surface and interface characteristics of CQD-based light-driven hydrogen production has dramatically improved in recent years.[12–15] Surface ligands, atom regulation and interface modification have been proven as vital tools to optimize the surface and interface properties of CQDs.[16–18] For instance, Tong *et al.* prepared AgInSe CQDs coated with a ZnSe passivation layer using the *in situ*-growth method and copper incorporation.[19] The photoelectrochemical performance of the optimized AgInSe core–shell CQDs delivered a maximum photocurrent density of 9.1 mA cm^{-2} under standard AM 1.5G illumination. Cai *et al.* proposed a unique method to tune the surface intragap states of $CuInS_2$ CQDs through surface

---

[a] *Quantum Research Center, Southwest Institute of Technical Physics, Chengdu 610041, China*

[b] *Institute of Fundamental and Frontier Sciences, University of Electronic Science and Technology of China, Chengdu 610054, China. E-mail: tong@uestc.edu.cn; 202011210301@std.uestc.edu.cn; hzsong@uestc.edu.cn*

[c] *Shimmer Center, Tianfu Jiangxi Laboratory, Chengdu 641419, China*

[d] *State Key Laboratory of High Power Semiconductor Lasers, Changchun University of Science and Technology, Changchun 130013, China*

† Mengke Cai and Shuai Huang are co-first author.

substitution and distribution of zinc incorporation,[20] facilitating slow hot electron relaxation and favoring long-lived charge separation. In addition, molecular iron and heterogeneous platinum co-catalysts loaded on CQDs were studied to improve charge carrier dynamics and chemical catalytic kinetics.[21,22] Notably, Li *et al.* recently designed a CdTe/In_2S_3 heterostructure photocatalyst to achieve a higher than 100% internal quantum efficiency by combining an interfacial built-in electric field and cascade energy band structure.[23]

In this review, we aim to provide valuable insights for understanding the surface and interface modification strategies for CQD-based light-driven hydrogen production, especially focusing on the core–shell structural design, passivation layer modification, surface ligand optimization, heterostructure construction, co-catalyst loading, and defect engineering of CQDs (Fig. 1). We first introduce the CQD-based photoelectrochemical and photocatalytic schemes for light-driven hydrogen production and comprehensively evaluate the advantages and disadvantages of the two technical solutions. Second, the surface and interface regulation of CQDs is systematically summarized, followed by the discussion of potential advancements and applications in related technologies. Finally, the last section of this review discusses perspectives on future trends and possible development directions for the surface and interface engineering for CQD-based light-driven hydrogen production.

Fig. 1 Overview of the surface and interface modification strategies discussed in this review.

2. CQD-based schemes for light-driven hydrogen production

Light-driven hydrogen generation systems are mainly classified into two categories based on the hydrogen production principle: indirect light-driven photovoltaic-electrolysis (PV-EC) hydrogen generation systems and direct light-driven hydrogen generation systems.[24,25] The latter can be further categorized into (i) photoelectrochemical cell (PEC) hydrogen generation systems relying on the photoelectrode; (ii) photocatalysis (PC) systems.[26–29] In the photoelectrochemical hydrogen generation systems, CQDs are typically integrated with wide-bandgap semiconductor films such as TiO_2.[30] Small size CQDs can be loaded onto the surface or pores of semiconductor films using chemical bath deposition or electrophoretic deposition methods.[31] In these systems, one side of the photoelectrode is connected to a charge collector, while the other side is in contact with the electrolyte. As illustrated in Fig. 2a, hydrogen gas and oxygen gas are produced on different electrodes.[32] Depending on the types of photoelectrodes used in hydrogen generation systems, photoelectrochemical hydrogen generation

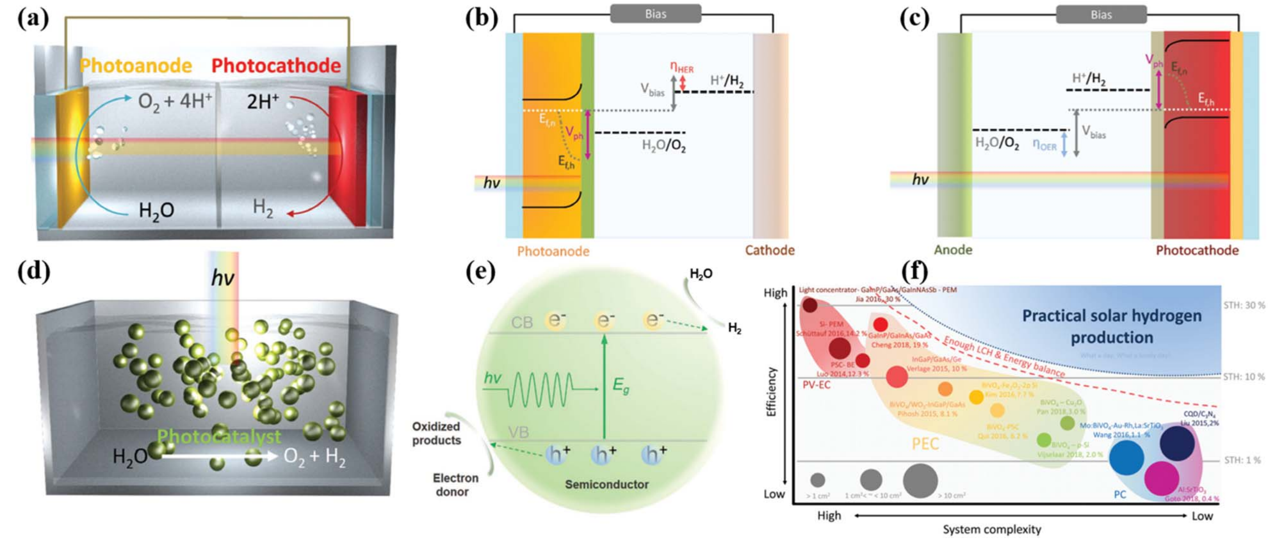

Fig. 2 Various direct light-driven hydrogen production systems and their charge flows upon light absorption. (a) PEC systems, (b) photoanode, (c) photocathode, (d) PC systems, (e) photocatalytic H_2 evolution using CQDs as light absorbers with surface atoms serving as the active sites for H^+ reduction. (f) Technological map showing various light-driven hydrogen production approaches for solar energy conversion. Reproduced with permission from ref. 32, copyright 2019, the Royal Society of Chemistry. Reproduced with permission from ref. 33, copyright 2022, John Wiley and Sons. Reproduced with permission from ref. 34, copyright 2018, Nature Publishing Group.

systems can be further categorized into photoanode and photocathode hydrogen generation systems.

Fig. 2b shows photoanode hydrogen generation systems. The N-type semiconductor, acting as the light absorber, forms a semiconductor–liquid junction with the electrolyte. In the case of upward bending of the band, photoexcited holes generated in the valence band participate in the water oxidation reaction to produce oxygen, while conduction band electrons overcome overpotential and voltage losses, getting transferred to the cathode to participate in the water reduction reaction to generate hydrogen. In contrast, the photocathode hydrogen generation systems require a P-type semiconductor as the light absorber. As shown in Fig. 2c, conduction band electrons induced by light radiation directly participate in the water reduction reaction to produce hydrogen. The PC system is similar to the PEC system as it spontaneously produces hydrogen without external bias. As illustrated in Fig. 2d, photocatalysts such as CQDs dispersed in a liquid or film can directly generate hydrogen gas molecules under light excitation.[33] Generally, CQD-based photocatalytic hydrogen generation involves three steps: (i) CQDs absorb photons, promoting electron transition from the valence band to the conduction band, leaving behind holes and forming electron–hole pairs. (ii) As shown in Fig. 2e, conduction band electrons and valence band holes migrate to the CQD surface, while some electron–hole pairs are annihilated through direct recombination or captured by defects. (iii) Photo-generated electrons on the semiconductor surface undergo a reduction reaction with surface-adsorbed water molecules or hydrogen ions, producing hydrogen gas. Photo-generated holes engage in an oxidation reaction with surface-adsorbed water molecules or hydroxide ions, generating oxygen gas. Usually, the PC system is simpler compared with the PEC system, as the charge transfer pathways of the photocatalytic system typically range from nanometers to millimeters, requiring a simpler device structure without the need for electrodes, charge collectors, or conductors utilized in the PEC system.

The most critical evaluation parameter for light-driven hydrogen generation performance is the solar-to-hydrogen energy conversion efficiency (η_{STH}), reflecting the ratio of produced hydrogen energy to incident solar energy under standard sunlight exposure without external bias.[35] The η_{STH} can be calculated from the rate of hydrogen evolution using eqn (1):

$$\eta_{\mathrm{STH}} = \frac{R_{\mathrm{H_2}}\ (\mu\mathrm{mol\ s^{-1}}) \times \Delta G_{\mathrm{r}}\ (\mathrm{kJ\ mol^{-1}})}{P_{\mathrm{light}}\ (\mathrm{mW\ cm^{-2}}) \times S\ (\mathrm{cm^2})}, \tag{1}$$

where $R_{\mathrm{H_2}}$ is the rate of hydrogen evolution, ΔG_{r} is the Gibbs energy (237.2 kJ mol^{-1}) for the reaction $H_2O(l) \rightarrow H_2(g) + 1/2O_2(g)$, P_{light} is the illumination intensity, and S is the total geometrical areas of the illumination.

There are some comprehensive points that should be noted to evaluate light-driven hydrogen production. The faradaic efficiency (FE), defined as the ratio of electrons consumed in hydrogen production to the total electrons transferred in the PEC system, is calculated as follows:

$$\mathrm{FE} = \left(\frac{2n_{\mathrm{H_2}}F}{Q}\right) \times 100\%, \tag{2}$$

where $n_{\mathrm{H_2}}$ is moles of H_2 produced, F is Faraday's constant (96 485 C mol^{-1}), and Q is the total charge passed. The incident photon-to-current efficiency (IPCE) is the percentage of incident photons converted into photoelectrons contributing to hydrogen production in the PEC system and is calculated at a specific wavelength (λ):

$$\mathrm{IPCE} = \left(\frac{1240 \times J_{\mathrm{light}}}{\lambda \times P_{\mathrm{light}}}\right) \times 100\%, \tag{3}$$

where J_{light} is the photocurrent density. A high IPCE value indicates effective light utilization. The turnover number (TON) is usually defined as the total moles of H_2 produced per active catalytic site:

$$\mathrm{TON} = \frac{n_{\mathrm{H_2}}}{n_{\mathrm{sites}}}. \tag{4}$$

The turnover frequency (TOF) measures intrinsic catalytic activity as H_2 production rate per active site:

$$\mathrm{TOF} = \frac{n_{\mathrm{H_2}}}{n_{\mathrm{sites} \times t}}, \tag{5}$$

where t is the reaction time. There are many other points, such as stability and light harvesting frequency, that researchers have to focus on during the exploration of light-driven hydrogen production.

As shown in Fig. 2f, the research trend of light-driven hydrogen production is clear and obvious.[34] PV-EC currently demonstrates higher efficiency values due to the rapid development of photovoltaic and electrolysis technology. However, considering the key factors of system complexity and cost, PEC and PC systems may be more suitable for future large-scale hydrogen production applications. Hence, both PEC and PC technologies offer research possibilities in balancing economic benefits and light-driven hydrogen production performance. Particularly, CQDs can be fabricated and processed in solution under mild conditions, enabling large-area manufacturing and widening the scope of low-cost hydrogen production technologies for the future hydrogen economy landscape.[36–43]

3. Surface and interface engineering for CQD-based light-driven hydrogen production

CQD-based PC hydrogen production and PEC hydrogen production follow the same pathway for photon–electron–proton energy transfer: (i) CQDs absorb photons, (ii) photogenerated charges separate, (iii) photogenerated charges migrate to the surface, (iv) photogenerated charges recombine at defects or the surface, and (v) photogenerated charges undergo redox reactions at the surface.[35] As illustrated in Fig. 3, the surface environment directly influences the energy transfer pathway. The key influencing factors for η_{STH} mainly include the light absorption efficiency (η_{Abs}), photogenerated charge separation efficiency (η_{Sep}), and interface transfer efficiency (η_{Transfer}) of photogenerated charges. As CQDs possess a high surface area and surface atomic ratios, surface and interface

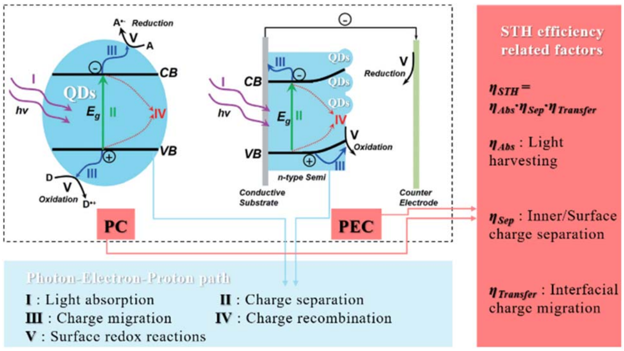

Fig. 3 Schematic of surface and interface factors for CQD-based light-driven hydrogen production. Reproduced with permission from ref. 35, copyright 2015, the Royal Society of Chemistry.

control of CQDs is a critical factor influencing their performance in light-driven hydrogen production.

Hence, surface and interface engineering of CQD were widely studied in terms of core–shell structural design, passivation layer modification, surface ligand optimization, heterostructure construction, co-catalyst loading, and defect engineering. It has been proved that the above strategies can promote charge separation, optimize interfacial reaction kinetics, and improve hydrogen production performance.

3.1 Core–shell structural design

Numerous studies have demonstrated that inorganic shells can protect CQDs from the influence of defect states, trap states, and chemical environments.[42,44] Therefore, constructing core–shell structures is an effective strategy to enhance the stability of CQDs and passivate surface defect states.[45] The construction of core–

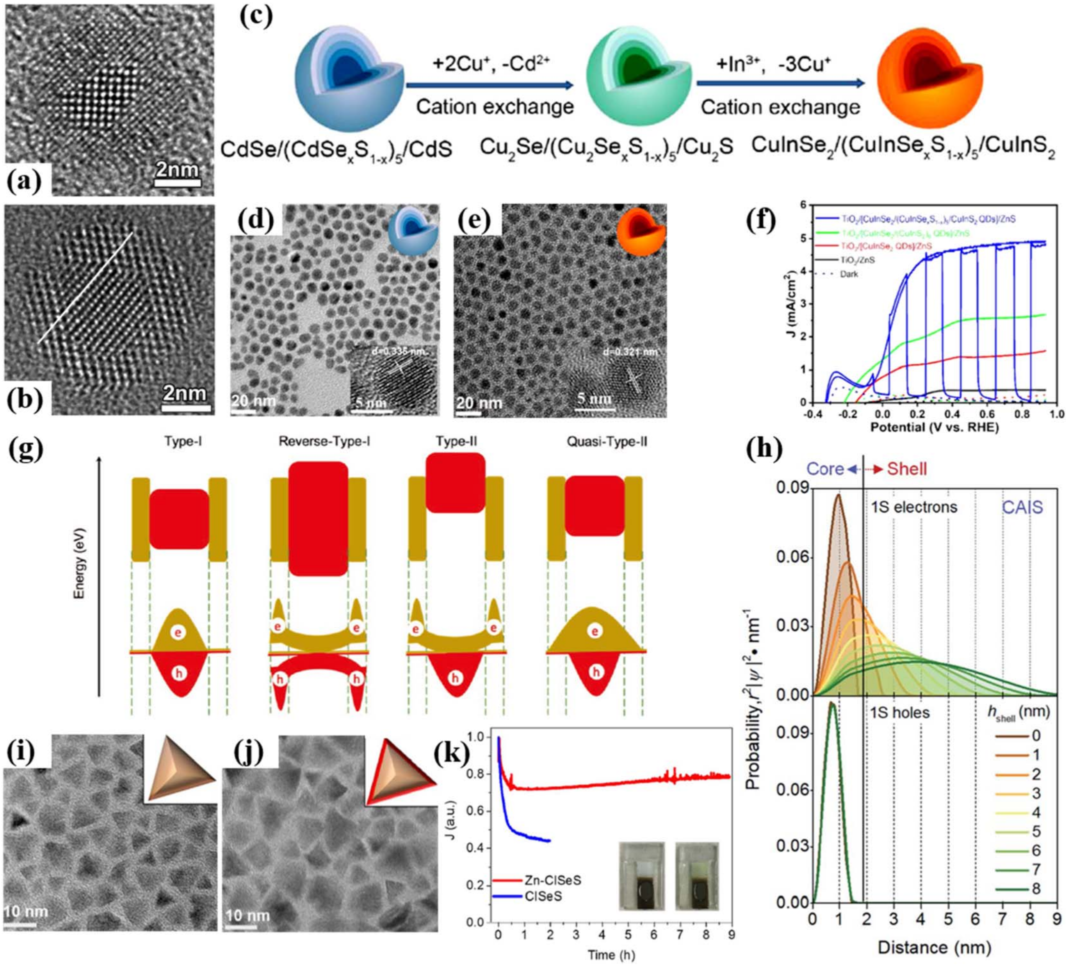

Fig. 4 Core–shell structural design and passivation layer modification. (a) TEM image of PbTe@CdTe in the [100] crystal axis direction. (b) TEM image of PbTe@CdTe in the [110] crystal axis direction. (c) Schematic of gradient multi-shell core–shell CQDs prepared using the SILAR method. (d) TEM image of $CdSe/(CdSe_xS_{1-x})_5/CdS$. (e) TEM image of $CuInSe_2/(CuInSe_xS_{1-x})_5/CuInS_2$. (f) Current–voltammetry curves of the gradient multi-shell core–shell CQD-sensitized TiO_2 photoanode. (g) Schematic of band arrangement and electron–hole spatial distribution wave functions of different core–shell CQDs. (h) Wave function diagram of electron–hole spatial distribution in $Cu–AgIn_5S_8@ZnS$ core–shell CQDs. (i) TEM image of $CuInSe_xS_{2-x}$. (j) TEM image of $CuInSe_xS_{2-x}$ with ZnS passivation. (k) Current–time curves of CQD-sensitized TiO_2 photoanode. Reproduced with permission from ref. 46, copyright 2009, American Chemical Society. Reproduced with permission from ref. 47, copyright 2020, John Wiley and Sons. Reproduced with permission from ref. 48, copyright 2020, the Royal Society of Chemistry. Reproduced with permission from ref. 49, copyright 2017, Elsevier.

shell CQDs primarily involves two methods: ion exchange and successive ionic layer adsorption and reaction (SILAR). As shown in Fig. 4a and b, Lambert *et al.* successfully prepared PbTe@CdTe core–shell CQDs with a typical core–shell structure characteristic using the cation exchange method:[46] PbTe core CQDs were first synthesized, purified and re-dispersed in toluene; then, core CQDs were introduced into oleylamine cadmium solution by controlling the reaction time to determine the thickness of the CdTe shell. Recently, Rosei *et al.* synthesized complex multi-shell core–shell CQDs using a combination of cation exchange and SILAR methods.[50] As shown in Fig. 4c, they first prepared CdSe/$(CdSe_xS_{1-x})_5$/CdS CQDs using SILAR layer by layer. Subsequently, they performed two cation exchanges by replacing Cd and introducing Cu and In cations, eventually forming gradient multi-shell core–shell $CuInSe_2/(CuInSe_xS_{1-x})_5/CuInS_2$ CQDs. The TEM images presented Fig. 4d and e confirm the successful preparation of special gradient multi-shell core–shell CQDs. The gradient shell layers facilitate the establishment of a gradual band alignment, which promotes the transfer of photo-induced charges. Ultimately, the sensitization of TiO_2 photoanodes by gradient multi-shell core–shell CQDs can enhance the photoelectrochemical hydrogen production performance by 3-fold and 1.7-fold compared with core and core–shell CQD-sensitized TiO_2 photoanodes, as shown in Fig. 4f.

Based on the bandgaps of the core and shell layers,[47] as well as the positions of the conduction band bottom and valence band top, core–shell CQDs can be classified into several types: type-I, reverse type-I, type-II, and quasi-type-II shown in Fig. 4g. In type-I core–shell CQDs, the effective bandgap of the shell layer is greater than that in core CQDs. The conduction band bottom and valence band top of the shell layer are located outside the bandgap of core CQDs. In this case, photo-induced charges are confined within the core CQDs, effectively enhancing radiation recombination efficiency and stability. Compared with type-I core–shell CQDs, reverse type-I core–shell CQDs exhibit a reversed band alignment, where the effective bandgap of the shell layer is smaller than that of the core CQDs, allowing both photo-induced electrons and holes to transfer to the shell layer. These core–shell quantum CQDs can efficiently consume photo-induced charges in the photocatalysis or photoelectrochemical process, thus enhancing photo-induced charge transfer efficiency. In typical type-II core–shell CQDs, the bandgaps of the core and shell layers are staggered, with photo-induced holes and electrons restricted to either the core or shell region. When the conduction band bottom or valence band top positions of the core and shell layers align, a quasi-type-II band alignment is formed. One of the photo-induced charges is delocalized at the aligned conduction band bottom or valence band top position, while the other photo-induced charge is restricted. Hence, the core–shell CQDs with quasi-type-II band alignment exhibit less overlap in the spatial distribution of electron–hole wave functions. For type-II and quasi-type-II core–shell CQDs, photo-induced charges can be effectively separated to reduce the probability of charge recombination, which is commonly applied in the fields of PC and PEC. For instance, Guo *et al.* designed ZnS shell layers with different thicknesses on the surface of Cu–$AgIn_5S_8$ CQDs, forming core–shell CQDs with type-II band alignment between the Cu–$AgIn_5S_8$ core and ZnS shell layers. To further analyze the spatial distribution of electron–hole wave functions for Cu–$AgIn_5S_8$@ZnS core–shell CQDs using theoretical calculation models,[48] it was demonstrated that the core–shell CQDs possessed a typical type-II band alignment structure. With increasing ZnS shell layer thickness, photo-induced electrons gradually delocalized from the core to the shell layer. As shown in Fig. 4h, photo-induced holes remained localized within the core, achieving effective charge separation of photo-induced charges. When Cu–$AgIn_5S_8$@ZnS core–shell CQDs were utilized to sensitize TiO_2 photoanodes, the photocurrent density increased by 1.5 times compared with Cu–$AgIn_5S_8$ core CQDs, verifying the excellent charge separation effect of the type-II band alignment structure.

3.2 Passivation layer modification

Compared with the core–shell structure, passivation layer modification involves growing ultra-thin inorganic or organic shell layers on the surface of CQDs with low atomic thicknesses.[51] The method usually does not alter the band structure of CQDs but provides weaker enhancement in stability compared with core–shell structures.[52] The primary function is to passivate surface defect states and inhibit photo-induced charge recombination.[53] For instance, Tong *et al.* developed an ultra-thin ZnS passivation shell layer on the surface of $CuInSe_xS_{2-x}$ CQDs through cation exchange,[49] as depicted in the TEM images (Fig. 4i and j). Ultraviolet-visible absorption spectroscopy indicated that the introduction of the ZnS passivation layer almost did not alter the bandgap of the core $CuInSe_xS_{2-x}$ CQDs. Photoluminescence results revealed that CQDs passivated with ZnS exhibited a longer average lifetime and stronger fluorescence emission intensity, indicating the ability of the ZnS shell layer to passivate surface defect states. Under standard sunlight conditions, $CuInSe_xS_{2-x}$ CQD sensitized-TiO_2 with ZnS passivation achieved a saturated photocurrent density of up to 4.62 mA cm^{-2}, significantly higher than that of bare $CuInSe_xS_{2-x}$ CQDs (2.57 mA cm^{-2}). Moreover, the improvement in stability can be observed from the current–time curves (Fig. 4k).

Additionally, Jin *et al.* reported that ultra-thin ZnS passivation layers could be deposited on the surface of PbS@CdS core–shell CQDs using the SILAR method, expanding the construction methods for passivation layers.[54] The work also provides valuable insights for optimizing the performance of the CQD-based photoelectrochemical hydrogen production system. Recently, Xia *et al.* conducted elemental incorporation in ZnSe-coated AgInSe CQDs with a passivation layer, which can tailor carrier kinetics for high-efficiency solar energy conversion.[19] The ZnSe passivation shell with Cu incorporation promoted the trapping of photoinduced holes from AgInSe QDs, resulting in a decelerated recombination of carriers. The prepared core–shell QDs with optimized optoelectronic properties were employed to fabricate QD-PEC devices, delivering a maximum photocurrent density of 9.1 mA cm^{-2} under standard AM 1.5G illumination. Moreover, the passivation layer prevented QDs from falling off substrates. Wang *et al.* reported that an ordered Al_2O_3 passive layer was deposited on the surface of silicon phosphide QDs through atomic layer deposition technology.[55] The layer can increase the bonding force between composite materials, thereby improving the stability of the device for photoelectrochemical water splitting.

3.3 Surface ligand optimization

Surface ligands not only stabilize CQDs but also act as an intermediate layer between the CQDs and the reaction medium, influencing photo-driven hydrogen production performance.[56–59] For instance, Reisner *et al.* synthesized ZnSe CQDs weakly coordinated with tetrafluoroborate ions (BF_4^-) and then capped the CQDs with 3-(2-mercaptoethyl)-1-methylimidazolium (MEMI) halides,[60] as shown in Fig. 5a. Owing to the similar strong affinity between BF_4^- and MEMI, the MEMI ligands can stably anchor to the surface of ZnSe CQDs. As a result, MEMI optimized the chemical environment of the CQD surface, modulated photocatalytic selectivity by inhibiting hydrogen evolution catalytic sites, and improved the selectivity for photocatalytic reduction. Furthermore, surface ligands can affect the self-assembly of CQDs and cocatalysts. As shown in Fig. 5b, Lu *et al.* prepared CdS CQDs capped with negatively charged mercaptopropionic acid (MPA) and neutral oleic acid (OLA).[61] When using positively charged homogeneous cocatalysts, ζ-potential measurements demonstrated that MPA–CdS CQDs could form electrostatic assemblies with homogeneous cocatalysts. During photocatalytic reduction in an aqueous phase, the catalytic TON of MPA–CdS reached 1380, while that of OLA–CdS was only 93, highlighting the significant impact of surface ligands on photocatalytic performance.

Recently, surface ligands have been found to influence the excited states of light absorption for CQDs.[66] For example, Asbury *et al.* utilized mid-infrared transient absorption spectroscopy to reveal the impact of the ligand structure on the absorption states at the CQD boundaries.[62] Fig. 5c illustrates the structures of PbS CQDs capped with OLA, MPA, and I$^-$ ions. The work determined successful ligand anchoring to the surface of CQDs through infrared spectroscopic characteristics of different ligands. Mid-infrared transient absorption spectroscopy indicated that the intensity of Pb–O coordination bonds on the surface of OLA-capped PbS CQDs decreased upon light excitation, reflecting an increase in the density of photoinduced electrons on the surface

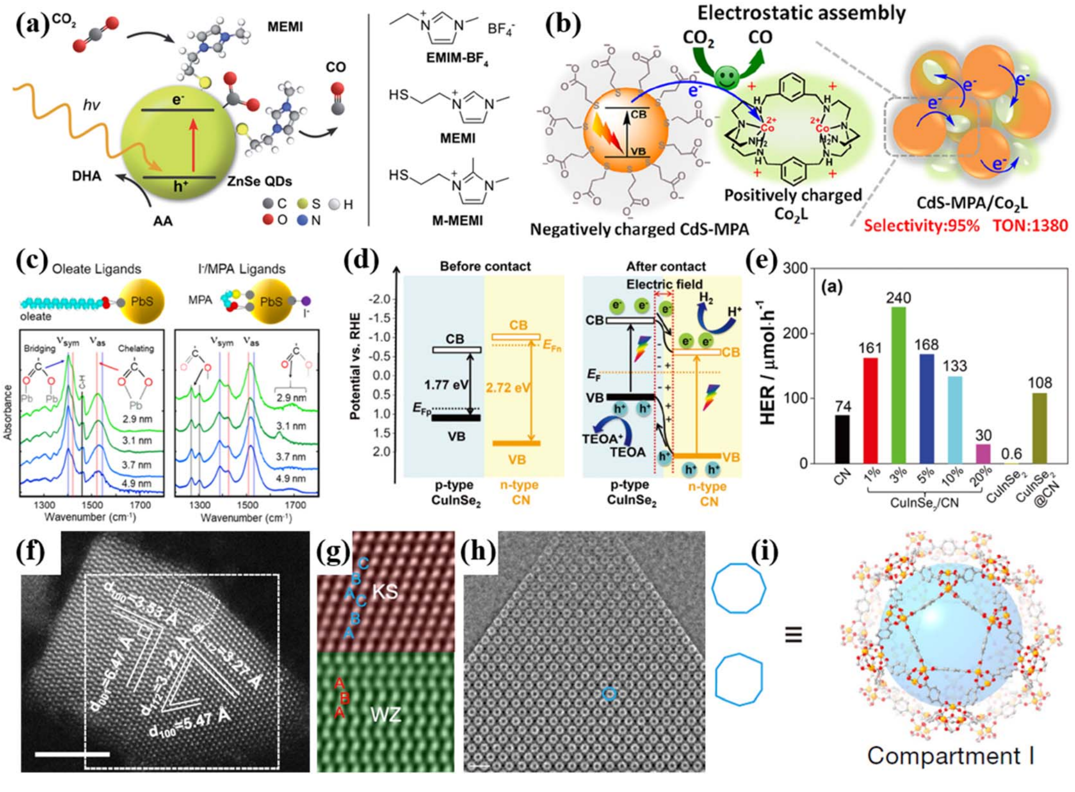

Fig. 5 Surface ligand optimization and heterostructure construction. (a) Schematic of ZnSe capped with the MEMI ligand. (b) Self-assembly of negatively charged MPA–CdS with positively charged co-catalysts through electrostatic interaction. (c) PbS capped with OLA, MPA, and I$^-$ ions along with the infrared spectrum. (d) Schematic of the heterojunction formed by p-type $CuInSe_2$ and n-type polymer CN. (e) Performance comparison of photocatalytic hydrogen production for $CuInSe_2$ and polymer CN. (f) HAADF-STEM image of the Cu_2ZnSnS_4 homojunction containing chalcopyrite and zinc blend phases. (g) Local magnified pseudo-color image within the rectangular frame in (f). (h) HAADF-STEM differential phase contrast image of MIL-101-Cr. (i) Schematic of pores filled with TiO_2 quantum dots. Reproduced with permission from ref. 60, copyright 2021, the Royal Society of Chemistry. Reproduced with permission from ref. 61, copyright 2018, American Chemical Society. Reproduced with permission from ref. 62, copyright 2021, American Chemical Society. Reproduced with permission from ref. 63, copyright 2020, the Royal Society of Chemistry. Reproduced with permission from ref. 64, copyright 2022, Nature Publishing Group. Reproduced with permission from ref. 65, copyright 2020, Nature Publishing Group.

of CQDs. Finally, this further affected the ligand mobility and catalytic activity at the interface. Conversely, I^-/MPA-capped PbS showed almost no change in the infrared absorption intensity for the surface coordination bonds. However, the energy transfer between neighboring CQDs and the localization of the photoinduced hole resulted in peak shifts in infrared absorption. Similarly, Patzke *et al.* reported S^{2-}-capped InP/ZnS core–shell CQDs with a short-chain inorganic ligand,[67] where S^{2-} ions could trap photoinduced holes of the InP/ZnS CQDs. Hence, the ligands reduced obstacles for photocarrier transfer and achieved adequate charge separation. Ultimately, the S^{2-}-capped InP/ZnS CQDs achieve a TON as high as 128 000 for photocatalytic hydrogen production, with a maximum internal quantum efficiency reaching 31%.

3.4 Heterostructure construction

Designing semiconductor heterojunctions has always been an effective strategy to improve the performance of light-driven hydrogen production.[68,69] The construction of semiconductor heterostructures primarily aims at enhancing the separation and transfer efficiency of photogenerated charges.[70–72] This strategy is equally applicable to CQDs and has been widely adopted in the past decade.[73] As shown in Fig. 5d, Lin *et al.* successfully constructed a PN junction by integrating P-type $CuInSe_2$ CQDs with N-type polymer carbon nitride (CN).[63] Owing to the formation of a built-in electric field in the interface, photogenerated electrons on the CQDs move to CN under the built-in electric field. Because of the energy band difference, the electron–hole pairs were effectively separated. Fig. 5e illustrates the light-driven hydrogen production performance for individual CQDs, polymer CN, and their composites under visible light irradiation. The composite photocatalyst with a PN junction shows a significant improvement in hydrogen production performance compared with individual photocatalysts.

In addition to heterojunction construction, Yu *et al.* successfully synthesized Cu_2ZnSnS_4 homojunctions containing wurtzite (WZ) and kesterite (KS) phases by regulating the synthesis temperature.[64] As shown in Fig. 5f, the high-angle annular dark-field scanning transmission electron microscopy image (HAADF-STEM) shows the coexistence of two different crystal phases within a single nanocrystal. As depicted in Fig. 5g, the locally enlarged HAADF-STEM image in the rectangular region clearly reveals the different atomic arrangements of the two phases. First-principle calculations and optical characterization revealed that the two phases in a single nanocrystal formed a type-II homojunction. Owing to the close contact through chemical bonding in the homojunction, photogenerated charges could be effectively separated.

CQD-based semiconductor heterojunctions have some unique advantages over other heterojunctions, benefiting from the unique optoelectronic properties, such as the multi-exciton effect and quantum tunneling effect.[74] For instance, Li *et al.* discovered that CdTe CQDs would generate high-energy hot electrons upon photon excitation exceeding the bandgap width,[23] then producing two pairs of electron–hole pairs through the multi-exciton effect. By utilizing this phenomenon, researchers achieved a maximum internal quantum efficiency of 118% in photocatalytic hydrogen production. Furthermore, Deng *et al.* reported the synthesis of uniformly sized TiO_2 quantum dots through confined growth within mesoporous metal–organic frameworks (MOFs) materials.[65] As shown in Fig. 5h and i, the HAADF-STEM differential phase contrast image of MIL-101-Cr, a type of MOF, demonstrates that the MOF possesses uniformly sized mesopores with a diameter of approximately 3.4 nm. In a confined growth environment, TiO_2 quantum dots nucleate and grow within the pores, creating a special CQD semiconductor heterojunction inside the porous material. Successfully applied in photocatalysis, the photogenerated electrons of TiO_2 CQDs can be stored in the adjacent metal nodes of the MOFs, ultimately achieving nearly a five-fold increase in apparent quantum efficiency.

3.5 Co-catalyst loading

The performance of light-driven hydrogen production is closely related to the involvement of electrons and holes in the oxidative and reductive reactions.[75] Therefore, from the perspective of chemical catalysis, loading hydrogen evolution cocatalysts on the surface of CQDs can optimize the catalytic kinetics of hydrogen production.[76,77]

Additionally, the introduction of cocatalysts can promote the separation of photogenerated charges on the surface of CQDs, preventing recombination of electron–hole pairs and extending the lifetime of photogenerated charges. As shown in Fig. 6a, Martindale *et al.* introduced a homogeneous Ni cocatalyst into water-soluble carbon CQDs.[78] The photogenerated electrons of the carbon CQDs can transfer to the molecular Ni cocatalyst to reduce protons and produce hydrogen molecules. Conversely, without the inclusion of the molecular Ni cocatalyst, carbon CQDs alone can hardly achieve photocatalytic hydrogen production. It is well known that noble metal Pt has been used as an excellent hydrogen evolution catalyst in industrial water electrolysis. Therefore, Wu *et al.* deposited Pt particles on the surface of CdS CQDs and studied the photocatalytic kinetics of CdS–Pt composite photocatalysts using femtosecond transient absorption (fs-TA) spectroscopy. They found that the average lifetime of ultrafast electron transfer from CdS to Pt is approximately 3.4 ps.[83] Additionally, owing to the confined photogenerated holes in CdS, the average lifetime of the separated photogenerated charge state is about 1.2 μs. Subsequently, Stolarczyk *et al.* deposited Pt particles at both ends of CdS nanowires, achieving spatial separation of photogenerated charges.[79] As shown in Fig. 6b, photogenerated electrons participate in the hydrogen evolution half-reaction at both ends of CdS nanowires, while photogenerated holes participate in the oxygen evolution half-reaction in the middle of CdS nanowires assisted by the homogeneous Ru cocatalyst. As depicted in Fig. 6c, fs-TA spectroscopy revealed the transfer lifetime of photogenerated charges. It can be observed that homogeneous cocatalysts exhibit a faster femtosecond-level lifetime of charge transfer compared with the heterogeneous cocatalyst. The TEM image in Fig. 6d also confirms that Pt particles were selectively deposited at both ends of CdS nanowires.

Furthermore, cocatalysts can be applied as the passivation shell on the surface of CQDs, optimizing catalytic kinetics and

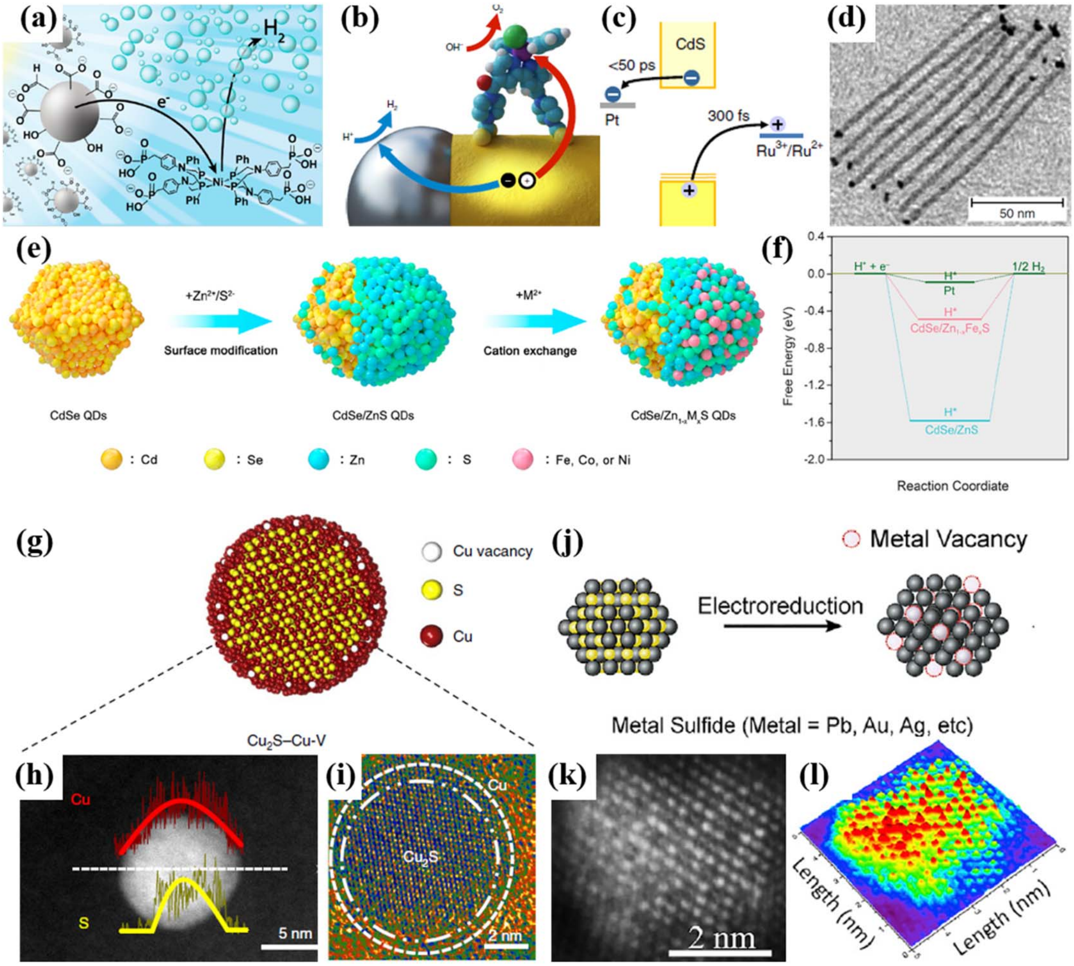

Fig. 6 Co-catalyst loading and defect engineering. (a) CQD-based photocatalytic hydrogen production with a homogeneous co-catalyst. (b) Schematic of hydrogen production by CdS assisted with a metal Pt co-catalyst. (c) Schematic of photogenerated charge transfer for CdS–Pt. (d) TEM image of CdS–Pt. (e) Construction of a $Zn_{1-x}M_xS$ co-catalyst layer *via* cation exchange. (f) Gibbs free energy calculation of the catalytic hydrogen evolution reaction for $CdSe/Zn_{1-x}Fe_xS$. (g) Schematic of Cu_2S–Cu–V CQDs with surface copper vacancy defects. (h) Energy spectrum line scan of Cu_2S–Cu–V. (i) High-resolution TEM image of Cu_2S–Cu–V. (j) Schematic of the CQD-derived catalyst with metal vacancy defects. (k) HAADF-STEM image of the CQD-derived catalyst. (l) Corresponding three-dimensional image of the CQD-derived catalyst. Reproduced with permission from ref. 78, copyright 2015, American Chemical Society. Reproduced with permission from ref. 79, copyright 2018, Nature Publishing Group. Reproduced with permission from ref. 80, copyright 2020, Elsevier. Reproduced with permission from ref. 81, copyright 2018, Nature Publishing Group. Reproduced with permission from ref. 82, copyright 2019, Elsevier.

passivating surface defects. As shown in Fig. 6e, Wu *et al.* recently used the cation exchange method to construct $Zn_{1-x}M_xS$ cocatalyst layers on the surface of CdSe/ZnS CQDs,[80] where M can be Fe, Co, or Ni. It was found that CdSe/ZnS CQDs covered with the $Zn_{1-x}M_xS$ cocatalyst layer exhibit superior photocatalytic hydrogen production performance compared with CdSe/ZnS CQDs. The density functional theory calculations also support the experimental conclusions presented in Fig. 6f. Compared with CdSe/ZnS CQDs, $CdSe/Zn_{1-x}Fe_xS$ CQDs exhibit lower Gibbs free energy for the intermediate H*, which is advantageous for optimizing the catalytic kinetics for hydrogen evolution reactions.

3.6 Defect engineering

CQDs are highly crystalline materials. However, defects are inevitably present on the surface of CQDs.[84,85] These defects are often considered recombination centers for photogenerated charges,[86–88] which hinder the transfer of photogenerated charges to reaction catalytic sites.[89,90] Surface defects typically cause structural relaxation in the local coordination environment.[91] It forms coordination-unsaturated sites that can affect the adsorption and activation of reactant molecules.[92] For instance, Sargent *et al.* locally reduced the surface atoms of Cu_2S CQDs to synthesize Cu_2S–Cu–V CQDs,[81] which were rich in copper vacancy defects, as shown in Fig. 6g. This confirmed the presence of copper vacancy defects through X-ray absorption tests and positron annihilation spectroscopy. As depicted in Fig. 6h, energy spectrum line scan data indicated that the surface is predominantly composed of copper with sulfur located internally, suggesting that Cu_2S exists in a core–shell form. This result was further supported by the TEM image (Fig. 6i). Experimental results along with Gibbs free energy calculations revealed that CQDs rich in copper vacancy defects could optimize the adsorption configuration of key transition states in reactions, thereby

Table 1 Comparison of various surface and interface engineering strategies for QD-based light-driven hydrogen production

Types of surface and interface engineering	QDs	PEC/PC system	Activity	STH	Stability	Ref.
Co-catalyst loading	CdSe	Photocathode	-2.14 mA cm^{-2} at 0 V *vs.* RHE	—	91.7% at 6 h	9
Surface ligand optimization	$ZnCuInS_2$	Photocathode	-0.68 mA cm^{-2} at 0 V *vs.* RHE	0.65%	99.9% at 2 h	14
Core–shell structural design	$CuInSe_2/ZnS$	Photoanode	6.0 mA cm^{-2} at 1.0 V *vs.* RHE	—	63% at 2 h	15
Defect engineering	$CuInSe_2$	Photoanode	10.7 mA cm^{-2} at 0.6 V *vs.* RHE	—	—	86
Surface ligand optimization	$ZnCuInS_2$	Photoanode	3.8 mA cm^{-2} at 1.23 V *vs.* RHE	0.54%	99.9% at 2 h	14
Core–shell structural design	$AgInS_2/ZnS$	Photoanode	6.4 mA cm^{-2} at 1.0 V *vs.* RHE	—	70% at 2 h	18
Passivation layer modification	$AgInSe_2$	Photoanode	9.1 mA cm^{-2} at 1.0 V *vs.* RHE	—	64% at 2 h	19
Co-catalyst loading	Ti_3C_2	Photoanode	2.9 mA cm^{-2} at 1.23 V *vs.* RHE	—	10 h	74
Core–shell structural design	MXene@Carbon	Photoanode	3.6 mA cm^{-2} at 1.23 V *vs.* RHE	—	8 h	75
Defect engineering	CuZnInSe	Photoanode	11.2 mA cm^{-2} at 0.8 V *vs.* RHE	—	61% at 2 h	86
Core–shell structural design	$AgInSe_2/ZnSe$	Photoanode	7.5 mA cm^{-2} at 1.0 V *vs.* RHE	—	70% at 2 h	36
Defect engineering	InP	Photoanode	7.4 mA cm^{-2} at 0.8 V *vs.* RHE	—	75% at 2 h	37
Heterostructure construction	$ZnAgInSe_2$	Photoanode	6.7 mA cm^{-2} at 0.9 V *vs.* RHE	—	71% at 1 h	38
Defect engineering	$ZnCuInS_2$	Photoanode	4.1 mA cm^{-2} at 0.6 V *vs.* RHE	—	76% at 1 h	39
Core–shell structural design	$AgGaS_2/CdSeS$	Photoanode	4.8 mA cm^{-2} at 0.9 V *vs.* RHE	—	—	40
Defect engineering	Mn–$CuInS_2$	Photoanode	5.7 mA cm^{-2} at 0.9 V *vs.* RHE	—	70% at 1 h	41
Core–shell structural design	$CuInS_2/CdS$	Photoanode	6.0 mA cm^{-2} at 0.8 V *vs.* RHE	—	78% at 1 h	42
Passivation layer modification	$AgInS_2$	Photoanode	5.7 mA cm^{-2} at 0.9 V *vs.* RHE	—	38% at 1 h	43
Heterostructure construction	CuInSeS	Photoanode	3.2 mA cm^{-2} at 1.23 V *vs.* RHE	0.69%	87% at 2 h	44
Core–shell structural design	CuInSe/CuInSeS/CuInS	Photoanode	4.5 mA cm^{-2} at 0.8 V *vs.* RHE	—	83% at 2 h	50
Core–shell structural design	$AgIn_5S_8/ZnS$	Photoanode	10.6 mA cm^{-2} at 0.7 V *vs.* RHE	—	50% at 2 h	48
Passivation layer modification	CuInSeS/CdSeS	Photoanode	5.3 mA cm^{-2} at 0.7 V *vs.* RHE	—	78% at 2 h	49
Core–shell structural design	PbS/CdS	Photoanode	11.2 mA cm^{-2} at 0.9 V *vs.* RHE	—	71% at 2 h	54
Surface ligand optimization	CdS	Photocatalyst	0.9 mmol g^{-1} h^{-1}	—	45 h	56
Surface ligand optimization	ZnSe	Photocatalyst	7.5 mmol g^{-1} h^{-1}	—	10 h	60
Surface ligand optimization	CdS	Photocatalyst	0.6 μmol h^{-1}	—	120 h	61
Core–shell structural design	InP/ZnS	Photocatalyst	15 μmol h^{-1}	—	100 h	67
Heterostructure construction	Zn–$AgIn_5S_8/Fe_2O_3$	Photocatalyst	1.7 mmol g^{-1} h^{-1}	—	36 h	68
Heterostructure construction	$CuInSe_2$	Photocatalyst	240 μmol h^{-1}	—	20 h	63
Heterostructure construction	Cu_2GaSnS_4	Photocatalyst	321 μmol g^{-1} h^{-1}	—	24 h	64
Co-catalyst loading	Carbon QDs	Photocatalyst	398 μmol g^{-1} h^{-1}	1.4%	28 h	78
Co-catalyst loading	CdS	Photocatalyst	23 μmol h^{-1}	—	20 h	79
Passivation layer modification	CdSe/ZnFeS	Photocatalyst	400 μmol h^{-1}	0.12%	60 h	80
Defect engineering	$ZnCuInS_2$	Photocatalyst	5.3 mmol g^{-1} h^{-1}	—	120 h	93
Heterostructure construction	$CuInS_2$	Photocatalyst	10.72 mmol g^{-1} h^{-1}	—	2 h	12
Defect engineering	$ZnCuInS_2$	Photocatalyst	50.4 mmol g^{-1} h^{-1}	—	24 h	20
Heterostructure construction	$ZnAgInS_2$	Photocatalyst	13.1 mmol g^{-1} h^{-1}	—	5 h	22
Heterostructure construction	CdTe	Photocatalyst	0.1 mmol h^{-1}	1.31%	100 h	23

modulating catalytic selectivity. In addition, Liu *et al.* constructed CQD-derived catalysts rich in metal vacancy defects from metal sulfide CQDs.[82] As depicted in Fig. 6j, CQD-derived catalysts containing metal Pb, Au or Ag defects could be prepared using this method. As shown in Fig. 6k and l, the HAADF-STEM images and their corresponding 3D representations clearly display metal defect sites, and extended X-ray absorption fine structure spectra (EXAFS) confirmed the formation of metal defects. This work features the modulation of surface atomic structure arising from the incorporation of defects and highlights the benefits of vacancy-rich metal catalysts for catalyst design and optimization. Recently, Cai *et al.* reported a class of defect-engineered copper deficient Zn-doped $CuInS_2$ CQDs,[93] which synergistically utilized copper vacancy and Cu^{2+} defect states. Transient optical characterizations revealed that copper vacancies can regulate the distribution of optically active defect states, wherein one defect state suppresses intra-band absorption and sharpens Shockley–Read–Hall recombination, while another defect state enable the prolonged exciton lifetime of CQDs.

3.7 The universality for surface and interface engineering

From the preceding discussion, it is evident that surface and interface engineering can effectively enhance the photo-driven hydrogen evolution performance of QDs. Notably, the abovementioned modification strategies exhibit universality across both photoelectrochemical and photocatalytic hydrogen production systems, including core–shell structural design, passivation layer modification, surface ligand optimization, heterostructure construction, co-catalyst loading and defect engineering. To further provide a comparative perspective, Table 1 categorizes and summarizes recent advances in surface and interface engineering for photo-driven hydrogen evolution. The analysis reveals two critical observations:

(1) These strategies are applicable to both PEC and PC hydrogen production systems.

(2) Current research predominantly focuses on photoanodes and photocatalytic systems, and rarely on photocathodes, which is largely owing to the lack of porous photocathode substrates capable of efficiently loading QDs.

In total, the surface and interface modification engineering of QDs has emerged as a pivotal technical approach to advancing photo-driven hydrogen evolution.

4. Conclusions and outlook

4.1 Conclusions

In summary, we have demonstrated that surface and interface engineering offer a promising approach to design light-driven hydrogen production systems, largely owing to their extensive and comprehensive benefits in providing photostability, dissociating electron–hole pairs, and optimizing catalytic kinetics. Additionally, these strategies provide critical and positive metrics for highly efficient solar-to-hydrogen conversion efficiency. Furthermore, CQD-based direct light-driven hydrogen production system offer well-balanced performance and cost for future industry-scale operation. The surface and interface properties can dramatically affect the electronic structure and the catalytic pathway. There are still many unexplored strategies that can modify the surface and interface of CQDs. For example, crystallographic engineering with special exposed crystal facets, as well as hydrophilic surface coverage, are highly efficient in water molecular adsorption and catalysis.

4.2 Perspective and challenges

Based on the above discussions, although significant progress has been made in regulating the surface and interface of CQDs, including combination of experimental methodologies and advanced characterization techniques, a number of fundamental challenges remain:

(1) More investigation needs to be undertaken to reveal the exact processes and mechanisms in view of the surface and interface of CQDs. Owing to the small size of CQDs, the local environment and state of surface and interface atoms are dynamically changed during the light-driven hydrogen production process, mainly because of photogenerated potential and solvent corrosion. Consequently, the precise identification of surface and interface sites and the exploration of mechanisms based on *ex situ* characterizations are impeded. Therefore, advanced *in situ* analytical techniques and *operando* microscopy should be applied to understand the surface and interface of CQDs. *In situ* TA is a powerful research tool to detect the surface defects of CQDs.

(2) The reported CQD-based light-driven hydrogen production systems still do not meet the requirements for commercial application, such as the target η_{STH} of over 10%. Nevertheless, possible strategies could involve the abovementioned surface and interface engineering to unlock the full potential of CQDs. For example, the combination of surface and interface engineering on a monolithic CQD-based light-driven hydrogen production system may provide an incredibly powerful and orthogonal toolbox.

(3) The stability of CQD-based light-driven hydrogen production system remains crucial. For a practical hydrogen production system, it is not the only key to focus on high activity for hydrogen production. Long-term stability of QD-based hydrogen production systems is critical for continuous solar to hydrogen fuel conversion. Despite the rational design of a variety of surface and interface engineering approaches to enhance the photostability of QDs and QD-based photoelectrodes, it is still the key weakness compared with other bulk semiconductor materials owing to relative general stability. More detailed and in-depth investigations of appropriate approaches should be exploited to further improve the stability while maintaining high activity.

Owing to emerging challenges and new opportunities, recent works have proposed collaborative strategies, simultaneously optimizing the core–shell layers and designing gradient doped structures. This will be crucial for advancing light-driven hydrogen production systems beyond CQD-based limitations.

Data availability

No primary research results, software or code has been included and no new data were generated or analysed as part of this review.

Author contributions

Conceptualization, M. C. and H.-Z. S.; resources, X. T. and H.-Z. S.; writing review and editing, M. C., Y. Y., S. H. H. J., J. Q., W. H., Z. L., Q. X., S. S., S. D. and W. Z.; supervision, H.-Z. S.; funding acquisition, H.-Z. S.; all the authors have read and agreed to the published version of the manuscript.

Conflicts of interest

There are no conflicts to declare.

Acknowledgements

This research was supported by the National Key Research and Development Program of China under the grant no. 2019YFB2203400 and no. 2021YFA0718803 and by the Natural Science Foundation of Sichuan Province under the grant no. 2022NSFSC1817. We also acknowledge the support of the Special Subject of Significant Science and Technology of Sichuan Province under grant 2018TZDZX0001 and the Special Subject of Significant Innovation of Chengdu City under grant 2021-YF08-00159-GX.

Notes and references

1 P. V. Kamat and K. Sivula, *ACS Energy Lett.*, 2022, **7**, 3149–3150.

2 H. Wu, H. L. Tan, C. Y. Toe, J. Scott, L. Wang, R. Amal and Y. H. Ng, *Adv. Mater.*, 2020, **32**, 1904717.

3 S. Akin, N. Arora, S. M. Zakeeruddin, M. Grätzel, R. H. Friend and M. I. Dar, *Adv. Energy Mater.*, 2020, **10**, 1903090.

4 T. Hisatomi, J. Kubota and K. Domen, *Chem. Soc. Rev.*, 2014, **43**, 7520–7535.

5 A. L. Efros and M. Rosen, *Annu. Rev. Mater. Sci.*, 2000, **30**, 475–521.

6 F. P. Garcia de Arquer, D. V. Talapin, V. I. Klimov, Y. Arakawa, M. Bayer and E. H. Sargent, *Science*, 2021, **373**, eaaz8541.

7 J.-T. Ru, C.-H. Tung and L.-Z. Wu, *Nano Res.*, 2024, **17**, 10259–10278.

8 C. Coughlan, M. Ibáñez, O. Dobrozhan, A. Singh, A. Cabot and K. M. Ryan, *Chem. Rev.*, 2017, **117**, 5865–6109.

9 H. Li, P. Wen, A. Hoxie, C. Dun, S. Adhikari, Q. Li, C. Lu, D. S. Itanze, L. Jiang, D. Carroll, A. Lachgar, Y. Qiu and S. M. Geyer, *ACS Appl. Mater. Interfaces*, 2018, **10**, 17129–17139.

10 M.-M. Chen, H.-G. Xue and S.-P. Guo, *Coord. Chem. Rev.*, 2018, **368**, 115–133.

11 S.-C. Zhu and F.-X. Xiao, *ACS Catal.*, 2023, **13**, 7269–7309.

12 R. Zhang, H. Wang, Y. Li, D. Wang, Y. Lin, Z. Li and T. Xie, *ACS Sustainable Chem. Eng.*, 2021, **9**, 7286–7297.

13 R. Guo, J. Meng, W. Lin, A. Liu, T. Pullerits, K. Zheng and J. Tian, *Chem. Eng. J.*, 2021, **403**, 126452.

14 M. Cai, X. Tong, H. Zhao, X. Li, Y. You, R. Wang, L. Xia, N. Zhou, L. Wang and Z. M. Wang, *Small*, 2022, **18**, 2204495.

15 R. Wang, X. Tong, Z. Long, A. I. Channa, H. Zhao, X. Li, M. Cai, Y. You, X. Sun and Z. Wang, *Nano Res.*, 2022, **15**, 7614–7621.

16 C. Xie, X. Lu, F. Deng, X. Luo, J. Gao and D. D. Dionysiou, *Chem. Eng. J.*, 2018, **338**, 591–598.

17 H. Zhao and F. Rosei, *Chem*, 2017, **3**, 229–258.

18 L. Xia, X. Tong, X. Li, A. I. Channa, Y. You, Z. Long, A. Vomiero and Z. M. Wang, *Chem. Eng. J.*, 2022, **442**, 136214.

19 L. Xia, X. Tong, Y. Yao, Z. Long, M. Cai, L. Jin, A. Vomiero and Z. M. Wang, *Nano Energy*, 2024, **122**, 109302.

20 M. Cai, X. Tong, H. Zhao, P. Liao, L. Pan, G. Li and Z. M. Wang, *Appl. Catal., B*, 2024, **343**, 123572.

21 P. Sharma, M. Sharma, M. Dearg, M. Wilding, T. J. A. Slater and C. R. A. Catlow, *Angew. Chem., Int. Ed.*, 2023, e202301239, DOI: 10.1002/anie.202301239.

22 F. Li, Y. Liu, B. Mao, L. Li, H. Huang, D. Zhang, W. Dong, Z. Kang and W. Shi, *Appl. Catal., B*, 2021, **292**, 120154.

23 Y. Zhang, Y. Li, X. Xin, Y. Wang, P. Guo, R. Wang, B. Wang, W. Huang, A. J. Sobrido and X. Li, *Nat. Energy*, 2023, **8**, 504–514.

24 X. M. C. Ta, R. Daiyan, T. K. A. Nguyen, R. Amal, T. Tran-Phu and A. Tricoli, *Adv. Energy Mater.*, 2022, **12**, 2201358.

25 B. J. Ng, L. K. Putri, X. Y. Kong, Y. W. Teh, P. Pasbakhsh and S. P. Chai, *Adv. Sci.*, 2020, **7**, 1903171.

26 M. Grätzel, *Nature*, 2001, **414**, 338–344.

27 A. Kudo and Y. Miseki, *Chem. Soc. Rev.*, 2009, **38**, 253–278.

28 M. Cai, Q. Liu, Z. Xue, Y. Li, Y. Fan, A. Huang, M.-R. Li, M. Croft, T. A. Tyson, Z. Ke and G. Li, *J. Mater. Chem. A*, 2020, **8**, 190–195.

29 M. Cai, Y. Zhang, Y. Zhao, Q. Liu, Y. Li and G. Li, *J. Mater. Chem. A*, 2020, **8**, 20386–20392.

30 Z. Li, A. I. Channa, Z. M. Wang and X. Tong, *Small*, 2023, **19**, 2305146.

31 Y. You, X. Tong, A. I. Channa, X. Li, C. Liu, H. Ye and Z. Wang, *EcoMat*, 2022, **4**, 12206.

32 J. H. Kim, D. Hansora, P. Sharma, J. W. Jang and J. S. Lee, *Chem. Soc. Rev.*, 2019, **48**, 1908–1971.

33 J. Liu, Z. Luo, X. Mao, Y. Dong, L. Peng, D. Sun-Waterhouse, J. V. Kennedy and G. I. N. Waterhouse, *Small*, 2022, **18**, 2204553.

34 X.-B. Li, C.-H. Tung and L.-Z. Wu, *Nat. Rev. Chem*, 2018, **2**, 160–173.

35 J. Li and N. Wu, *Catal. Sci. Technol.*, 2015, **5**, 1360–1384.

36 Z. Long, X. Tong, R. Wang, A. I. Channa, X. Li, Y. You, L. Xia, M. Cai, H. Zhao and Z. M. Wang, *ChemSusChem*, 2022, **15**, 202200346.

37 H. Zhao, X. Li, M. Cai, C. Liu, Y. You, R. Wang, A. I. Channa, F. Lin, D. Huo, G. Xu, X. Tong and Z. M. Wang, *Adv. Energy Mater.*, 2021, **11**, 2101230.

38 Z. Long, X. Tong, C. Liu, A. I. Channa, R. Wang, X. Li, F. Lin, A. Vomiero and Z. M. Wang, *Chem. Eng. J.*, 2021, **426**, 131298.

39 C. Liu, X. Tong, A. I. Channa, X. Li, Z. Long, H. Feng, Y. You, R. Wang, F. Lin, C. F. Dee, A. Vomiero and Z. M. Wang, *J. Mater. Chem. A*, 2021, **9**, 5825–5832.

40 X. Li, X. Tong, S. Yue, C. Liu, A. I. Channa, Y. You, R. Wang, Z. Long, Z. Zhang, Z. Zhao, X.-F. Liu and Z. M. Wang, *Nano Energy*, 2021, **89**, 106392.

41 R. Wang, X. Tong, A. I. Channa, Q. Zeng, J. Sun, C. Liu, X. Li, J. Xu, F. Lin, G. S. Selopal, F. Rosei, Y. Zhang, J. Wu, H. Zhao, A. Vomiero, X. Sun and Z. M. Wang, *J. Mater. Chem. A*, 2020, **8**, 10736–10741.

42 C. Wang, X. Tong, W. Wang, J. Y. Xu, L. V. Besteiro, A. I. Channa, F. Lin, J. Wu, Q. Wang, A. O. Govorov, A. Vomiero and Z. M. Wang, *ACS Appl. Mater. Interfaces*, 2020, **12**, 36277–36286.

43 X. Tong, A. I. Channa, Y. You, P. Wei, X. Li, F. Lin, J. Wu, A. Vomiero and Z. M. Wang, *Nano Energy*, 2020, **76**, 105062.

44 M. Cai, X. Li, H. Zhao, C. Liu, Y. You, F. Lin, X. Tong and Z. M. Wang, *ACS Appl. Mater. Interfaces*, 2021, **13**, 50046–50056.

45 K. Wang, C. Wang, Y. Tao, Z. Tang, D. Benetti, F. Vidal, Y. Liu, M. H. Rummeli, H. Zhao, F. Rosei and X. Sun, *Adv. Funct. Mater.*, 2024, **34**, 2400580.

46 K. Lambert, B. D. Geyter, I. Moreels and Z. Hens, *Chem. Mater.*, 2009, **21**, 778–780.

47 G. S. Selopal, H. Zhao, Z. M. Wang and F. Rosei, *Adv. Funct. Mater.*, 2020, **30**, 1908762.

48 H. Guo, B. Luo, J. Wang, B. Wang, X. Huang, J. Yang, W. Gong, Y. Zhou and X. Niu, *J. Mater. Chem. A*, 2020, **8**, 24655–24663.

49 X. Tong, Y. Zhou, L. Jin, K. Basu, R. Adhikari, G. S. Selopal, X. Tong, H. Zhao, S. Sun, A. Vomiero, Z. M. Wang and F. Rosei, *Nano Energy*, 2017, **31**, 441–449.

50 F. Li, M. Zhang, D. Benetti, L. Shi, L. V. Besteiro, H. Zhang, J. Liu, G. S. Selopal, S. Sun, Z. Wang, Q. Wei and F. Rosei, *Appl. Catal., B*, 2021, **280**, 119402.

51 Q. Zheng, J. Wang, F. Huang, Z. Huang, S. Tian, Q. Chen, Y. Pei, K. Zheng and J. Tian, *ACS Energy Lett.*, 2024, **9**, 2358–2366.

52 A. I. Channa, Z. Li, L. Xia, X. Li, Z. M. Wang and X. Tong, *ACS Mater. Lett.*, 2024, **6**, 4517–4525.

53 H. Zhang, J. Liu, L. V. Besteiro, G. S. Selopal, Z. Zhao, S. Sun and F. Rosei, *Small*, 2024, **20**, 2306203.

54 L. Jin, B. AlOtaibi, D. Benetti, S. Li, H. Zhao, Z. Mi, A. Vomiero and F. Rosei, *Adv. Sci.*, 2016, **3**, 1500345.

55 S. Zhang, T. Yu, Y. Liu, M. Feng, X. Li, W. Sun and D. Wang, *Chem. Eng. J.*, 2022, **429**, 132248.

56 Y. X. Feng, H. J. Wang, J. W. Wang, W. Zhang, M. Zhang and T. B. Lu, *ACS Appl. Mater. Interfaces*, 2021, **13**, 26573–26580.

57 E. A. Weiss, *ACS Energy Lett.*, 2017, **2**, 1005–1013.

58 S. Lian, M. S. Kodaimati and E. A. Weiss, *ACS Nano*, 2018, **12**, 568–575.

59 M. S. Kodaimati, S. Lian, G. C. Schatz and E. A. Weiss, *Proc. Natl. Acad. Sci. U. S. A.*, 2018, **115**, 8290–8295.

60 C. D. Sahm, E. Mates-Torres, N. Eliasson, K. Sokołowski, A. Wagner, K. E. Dalle, Z. Huang, O. A. Scherman, L. Hammarström, M. García-Melchor and E. Reisner, *Chem. Sci.*, 2021, **12**, 9078–9087.

61 Q.-Q. Bi, J.-W. Wang, J.-X. Lv, J. Wang, W. Zhang and T.-B. Lu, *ACS Catal.*, 2018, **8**, 11815–11821.

62 E. R. Kennehan, K. T. Munson, C. Grieco, G. S. Doucette, A. R. Marshall, M. C. Beard and J. B. Asbury, *J. Am. Chem. Soc.*, 2021, **143**, 13824–13834.

63 Y. Zheng, Y. Chen, L. Wang, M. Tan, Y. Xiao, B. Gao and B. Lin, *Dalton Trans.*, 2020, **49**, 7598–7604.

64 L. Wu, Q. Wang, T. T. Zhuang, G. Z. Zhang, Y. Li, H. H. Li, F. J. Fan and S. H. Yu, *Nat. Commun.*, 2022, **13**, 5414.

65 Z. Jiang, X. Xu, Y. Ma, H. S. Cho, D. Ding, C. Wang, J. Wu, P. Oleynikov, M. Jia, J. Cheng, Y. Zhou, O. Terasaki, T. Peng, L. Zan and H. Deng, *Nature*, 2020, **586**, 549–554.

66 A. Cheruvathoor Poulose, G. Zoppellaro, I. Konidakis, E. Serpetzoglou, E. Stratakis, O. Tomanec, M. Beller, A. Bakandritsos and R. Zboril, *Nat. Nanotechnol.*, 2022, **17**, 485–492.

67 S. Yu, X. B. Fan, X. Wang, J. Li, Q. Zhang, A. Xia, S. Wei, L. Z. Wu, Y. Zhou and G. R. Patzke, *Nat. Commun.*, 2018, **9**, 4009.

68 D. Zhang, B. Mao, D. Li, Y. Liu, F. Li, W. Dong, T. Jiang and W. Shi, *Chem. Eng. J.*, 2021, **417**, 128275.

69 Z. K. Xin, Y. J. Gao, Y. Gao, H. W. Song, J. Zhao, F. Fan, A. D. Xia, X. B. Li, C. H. Tung and L. Z. Wu, *Adv. Mater.*, 2022, **34**, 2106662.

70 P. Wu, H. Liu, Z. Xie, L. Xie, G. Liu, Y. Xu, J. Chen and C.-Z. Lu, *ACS Appl. Mater. Interfaces*, 2024, **16**, 16601–16611.

71 Z. Huang, P. Sun, H. Zhang, H. Zhang, S. Zhang, Z. Chen, X. Yi and S. Xie, *ACS Catal.*, 2024, **14**, 4581–4592.

72 G. Sun, Z. Tai, J. Zhang, B. Cheng, H. Yu and J. Yu, *Appl. Catal., B*, 2024, **358**, 124459.

73 W. Shi, B. Ge, P. Jiang, Q. Wang, L. He and C. Huang, *Appl. Catal., B*, 2024, **354**, 124121.

74 R. Tang, S. Zhou, C. Li, R. Chen, L. Zhang, Z. Zhang and L. Yin, *Adv. Funct. Mater.*, 2020, **30**, 2000637.

75 D. N. Nguyen, G. S. Gund, M. G. Jung, S. H. Roh, J. Park, J. K. Kim and H. S. Park, *ACS Nano*, 2020, **14**, 17615–17625.

76 D. Zhou, Z. Cai, X. Lei, W. Tian, Y. Bi, Y. Jia, N. Han, T. Gao, Q. Zhang, Y. Kuang, J. Pan, X. Sun and X. Duan, *Adv. Energy Mater.*, 2018, **8**, 1701905.

77 Z. Zhou, C. Chen, M. Gao, B. Xia and J. Zhang, *Green Chem.*, 2019, **21**, 6699–6706.

78 B. C. Martindale, G. A. Hutton, C. A. Caputo and E. Reisner, *J. Am. Chem. Soc.*, 2015, **137**, 6018–6025.

79 C. M. Wolff, P. D. Frischmann, M. Schulze, B. J. Bohn, R. Wein, P. Livadas, M. T. Carlson, F. Jäckel, J. Feldmann, F. Würthner and J. K. Stolarczyk, *Nat. Energy*, 2018, **3**, 862–869.

80 Y.-J. Gao, X.-B. Li, X.-Z. Wang, N.-J. Zhao, Y. Zhao, Y. Wang, Z.-K. Xin, J.-P. Zhang, T. Zhang, C.-H. Tung and L.-Z. Wu, *Matter*, 2020, **3**, 571–585.

81 T.-T. Zhuang, Z.-Q. Liang, A. Seifitokaldani, Y. Li, P. De Luna, T. Burdyny, F. Che, F. Meng, Y. Min, R. Quintero-Bermudez, C. T. Dinh, Y. Pang, M. Zhong, B. Zhang, J. Li, P.-N. Chen, X.-L. Zheng, H. Liang, W.-N. Ge, B.-J. Ye, D. Sinton, S.-H. Yu and E. H. Sargent, *Nat. Catal.*, 2018, **1**, 421–428.

82 M. Liu, M. Liu, X. Wang, S. M. Kozlov, Z. Cao, P. De Luna, H. Li, X. Qiu, K. Liu, J. Hu, C. Jia, P. Wang, H. Zhou, J. He, M. Zhong, X. Lan, Y. Zhou, Z. Wang, J. Li, A. Seifitokaldani, C. T. Dinh, H. Liang, C. Zou, D. Zhang, Y. Yang, T.-S. Chan, Y. Han, L. Cavallo, T.-K. Sham, B.-J. Hwang and E. H. Sargent, *Joule*, 2019, **3**, 1703–1718.

83 K. Wu, H. Zhu, Z. Liu, W. Rodriguez-Cordoba and T. Lian, *J. Am. Chem. Soc.*, 2012, **134**, 10337–10340.

84 J. S. Park, S. Kim, Z. Xie and A. Walsh, *Nat. Rev. Mater.*, 2018, **3**, 194–210.

85 E. Pastor, M. Sachs, S. Selim, J. R. Durrant, A. A. Bakulin and A. Walsh, *Nat. Rev. Mater.*, 2022, **7**, 503–521.

86 S. Li, S.-M. Jung, W. Chung, J.-W. Seo, H. Kim, S. I. Park, H. C. Lee, J. S. Han, S. B. Ha, I. Y. Kim, S.-I. In, J.-Y. Kim and J. Yang, *Carbon Energy*, 2023, **5**, e384.

87 X. Chen, Y. Guo, J. Li, H. Yang, Z. Chen, D. Luo and X. Liu, *Chem. Eng. J.*, 2024, **496**, 153947.

88 W. Ullah, A. Slassi, C. Wang, E. Paineau, M.-H. Ha-Thi, T. Pino, Z. Halime, A. Gayral, M. Vallet, J. Degrouard, J. Cornil and M. N. Ghazzal, *Adv. Energy Mater.*, 2024, **14**, 2401547.

89 B. Luo, J. Liu, H. Guo, X. Liu, R. Song, K. Shen, Z. M. Wang, D. Jing, G. S. Selopal and F. Rosei, *Nano Energy*, 2021, **88**, 106220.

90 W. Li, R. Long, J. Tang and O. V. Prezhdo, *J. Phys. Chem. Lett.*, 2019, **10**, 3788–3804.

91 A. Kumar and V. Krishnan, *Adv. Funct. Mater.*, 2021, **31**, 2009807.

92 J. Xiong, J. Di, J. Xia, W. Zhu and H. Li, *Adv. Funct. Mater.*, 2018, **28**, 1801983.

93 M. Cai, X. Tong, P. Liao, S. Shen, H. Zhao, X. Li, L. Xia, H. Zhi, N. Zhou, Z. Xue, L. Jin, J. Li, G. Li, F. Dong, A. V. Kabashin and Z. M. Wang, *ACS Catal.*, 2023, **13**, 15546–15557.